Tensor Regression and Image Fusion-Based Change Detection Using Hyperspectral and Multispectral Images

Tianming Zhan, Yanwen Sun, Yongsheng Tang, Yang Xu, and Zebin Wu, *Senior Member, IEEE*

***Abstract*—Change detection is a popular topic in remote sensing that is generally constrained to two remote sensing images captured at two different times. However, the optimal type of remote sensing image for change detection tasks has not yet been determined. The use of only hyperspectral images (HSIs) with low spatial resolution or multispectral images (MSIs) with low spectral resolution cannot obtain satisfactory change detection results. In this article, we propose the fusion of simultaneously captured low spatial resolution HSIs and low spectral resolution MSIs with the use of a tensor regression-based method to detect change regions from the fused images at two different time points. In this method, nonlocal couple tensor CP decomposition is initially applied to fuse the HSIs and MSIs. A difference image is then obtained by subtracting the fused images at two different time points. Thereafter, the tensors are extracted from the difference image and the tensor regression-based method is used to classify the difference image and detect the final change results. Experimental results from three real datasets suggest that the proposed method substantially outperforms the existing state-of-the-art change detection methods as well as any change detection methods using single-source images.**

***Index Terms*—Change detection, hyperspectral images (HSIs), image fusion, multispectral images (MSIs), tensor regression.**

I. Introduction

CHANGE detection refers to calculating the difference between images captured in the same area at different time points via image processing and mathematical modeling techniques [1]–[5]. Change detection based on remote sensing images is a multidisciplinary technology involving geographic science, statistical science, and computer science and represents a popular research topic in the field of remote sensing [6]–[16]. Although remote sensing image change detection methods have been widely studied, several challenges remain, such as remote sensing images containing noise, blur, and other degradation problems due to the various structures of ground features, atmospheric radiation, and other factors. Beside this, spectral variability also make it difficult for spectral unmixing or object detection [17]. Thus, relying solely on spectral information is not sufficient to distinguish different objects [18]–[20]. Spectral-spatial fusion based methods are wildly used in hyperspectral image (HSI) processing field [21]–[23]. For example, Hong *et al.* [24] proposed a novel linearized subspace analysis technique with spatial-spectral manifold alignment for hyperspectral dimensionality reduction, and overcome the drawbacks in explainability, cost effectiveness, generalization capability, and representability of conventional nonlinear subspace learning.

At present, HSIs and multispectral images (MSIs) are often used for change detection. However, using only HSIs with low spatial resolution or MSIs with low spectral resolution cannot obtain satisfactory change detection results. Additionally, the remote sensing images collected during different periods may be captured by different sensing devices, and their spatial and spectral resolutions may be inconsistent [25]. To accurately detect change areas in remote sensing images, it is very important to fuse remote sensing images from different periods to achieve the same spatial and temporal resolutions [26]–[27].

In recent years, fusing HSIs and MSIs to improve resolution has attracted much attention. The most popular fusion methods include fusion algorithms based on component replacement [28], detail injection methods [29], spectral unmixing methods [30], deep learning methods [31]–[33], and tensor representation-based methods [34]–[36]. The main idea behind the tensor representation-based fusion method involves treating high-dimensional remote sensing images as a high-order tensor and using tensor decomposition technology and a regularization method to achieve high-dimensional image fusion. Li *et al.* [37] proposed a new HSI fusion method based on non-local sparse tensor decomposition. This method initially gathers similar hyperspectral blocks into a cluster, with similar blocks sharing the same dictionary. Each cluster learns a spectral dictionary

Manuscript received June 27, 2021; revised August 24, 2021; accepted September 21, 2021. Date of publication September 24, 2021; date of current version October 8, 2021. This work was supported in part by the National Natural Science Foundation of China under Grant 61976117 and Grant 62071233, in part by the Natural Science Foundation of Jiangsu Province under Grant BK20191409, in part by the Key Projects of University Natural Science Fund of Jiangsu Province under Grant 19KJA360001, in part by "Qinglan Project" of Jiangsu Universities; in part by the Fundamental Research Funds for the Central Universities, under Grant 30917015104, Grant 30919011103, and Grant 30919011402, in part by the Collaborative Innovation Center of Audit Information Engineering and Technology under Grant 18CICA09, in part by the Young Teacher Research and Cultivation Project of Nanjing Audit University under Grant 18QNPY015, and in part by the Postgraduate Research & Practice Innovation Program of Jiangsu Province under Grant KYCX21_1944. *(Corresponding author: Zebin Wu.)*

Tianming Zhan is with the Jiangsu Key Construction Laboratory of Audit Information Engineering, Nanjing Audit University, Nanjing 211815, China School of Information Engineering, Nanjing Audit University, Nanjing 211815, China (e-mail: ztm@nau.edu.cn).

Yanwen Sun and Yongsheng Tang are with the School of Information Engineering, Nanjing Audit University, Nanjing 211815, China (e-mail: mg2009111@stu.nau.edu.cn; mz2009118@stu.nau.edu.cn).

Yang Xu and Zebin Wu are with the Nanjing University of Science and Technology, Nanjing 210094, China (e-mail: xuyangth90@njust.edu.cn; zebin.wu@gmail.com).

Digital Object Identifier 10.1109/JSTARS.2021.3115345

from a low-resolution HSI as well as a wide-height dictionary from a high-resolution MSI. Then, each cluster learns the core tensor via the sparse coding of each block to ultimately complete a super-resolution hyperspectral reconstruction. Furthermore, Kanatsoulis *et al*. [38] proposed a joint dictionary decomposition framework for remote sensing image fusion using the multidimensional structure of HSIs and MSIs. This method can ensure the high discrimination of fusion results in practical applications without requiring additional prior knowledge of the degradation calculations. Xu *et al*. [39] proposed an HSI fusion method based on the sparse representation of nonlocal block tensors (NCTCP). This method combines tensor product-based sparse representation, tensor dictionary learning, nonlocal similarity prior, HSI and MSI image correlation, and other factors to construct an HSI fusion objective function and achieve a good fusion effect.

With the continuous development of remote sensing image change detection research, a wide variety of research results is constantly emerging. At present, change detection has evolved from simple mathematical operations [40]–[42] to the fusion of multiple methods [43]–[45] ranging from pixel-based change detection [46]–[49] to object-based change detection [50]–[54]. Such fusion-based change detection methods are divided into two main groups: feature level fusion and decision level fusion. The feature level fusion-based methods extract the change information by means of multitemporal images fusion. The decision level fusion based methods elaborate the information fusion at the level of decision [4]. Notably, the accuracy and complexity of change detection methods are constantly increasing. However, most existing change detection methods convert high-dimensional images into a matrix, which destroys the intrinsic structure of remote sensing images [55]. On the other hand, the theory and technology of tensor representation [56]–[59] have developed rapidly. Remote sensing images represent a natural high-order tensor form, and the tensor representation method is particularly suitable for image processing in remote sensing.

Based on the aforementioned information, it is known that: HSI and MSI fusion can improve image resolution and the accuracy of change detection; and a tensor form can avoid breaking the original structure of high-dimensional data and helps to improve change detection accuracy. In this article, we propose a tensor regression- and image fusion-based change detection method (TRIFCD) using HSIs and MSIs. To achieve this, NCTCP is initially applied to perform HSI and MSI fusion. Then, the difference image is obtained by subtracting the fused images at two different time points. Thereafter, the tensors are extracted from the difference image and a tensor regression-based method [51], [60] is used to classify the difference image to detect the final change results. The experimental results for three simulated datasets suggest that the proposed method substantially outperforms existing state-of-the-art change detection methods as well as any change detection methods using single-source images. In summary, the proposed method makes the following contributions.

1) It effectively couples the two tasks of image fusion and change detetion in a unified tensor-based framework.
2) It fully excavates and effectively uses hyperspectral and multispectral data to improve the accuracy of change detection.
3) The tensor representation method can maintain spectral-spatial information and overcome the effects of image degradation. Beside this, our method is no need for better hardware resources such as GPU to train the model.
4) The use of a simple and stable tensor regression classifier can obtain change detection results more accurately and efficiently.

II. Tensor Notations and Problem Formulation

A. Tensor Notations

According to [39], a tensor $\mathcal{A} \in \Re^{n_1 \times n_2 \times \cdots \times n_t}$is a multidimensional array. Thus, a matrix A is a 2-D tensor and vector a is a 1-D tensor. The 3-D data $\mathcal{X} \in \Re^{n_1 \times n_2 \times n_3}$ can be defined as a third-order tensor, and its horizontal, lateral, and frontal slices are denoted as $\mathcal{X}(k,:,:)$, $\mathcal{X}(:,k,:)$, and $\mathcal{X}(:,:,k)$, respectively. The (i,j)th mode-1, mode-2, and mode-3 fibers are denoted as $\mathcal{X}(:,i,j)$, $\mathcal{X}(i,:,j)$, and $\mathcal{X}(i,j,:)$. For the sake of clarity, we use $\mathcal{X}_{(k)}$ to represent the mode-k unfolding of $\mathcal{X}$ since $\mathrm{unfold}_i(\mathcal{X}) = X_{(i)}$ and $\mathcal{X} = \mathrm{fold}_i\,(X_{(i)})$.

The inner product of two third-order tensors $\mathcal{X}, \mathcal{Y} \in \Re^{n_1 \times n_2 \times n_3}$ is given as follows:

$$\langle \mathcal{X}, \mathcal{Y} \rangle = \sum_{i=1}^{n_3} \langle \mathcal{X}^{(i)}, \mathcal{Y}^{(i)} \rangle \tag{1}$$

where the inner product of second-order tensors X and Y is defined as $\langle X, Y \rangle = \mathrm{Trace}(\boldsymbol{X^T} Y)$and the inner product of first-order tensors x and y is defined as $\langle x, y \rangle = \mathrm{Trace}(x^T y)$.

The Frobenius norm of a third-order tensor $\mathcal{X}$ is defined as

$$\|\mathcal{X}\|_F = \left(\sum_{i,j,k} |\mathcal{X}(i,j,k)|^2 \right)^{1/2}. \tag{2}$$

B. HSI-MSI Fusion

Notably, HSIs have a higher spectral resolution but lower spatial resolution. Conversely, MSIs have a lower spectral resolution but higher spatial resolution. Thus, we can consider performing HSI-MSI fusion to obtain high-resolution spectral and spatial images. Here, we use $\mathcal{I} \in \Re^{w \times h \times B}$ to represent the observed HSI with a low spatial resolution (LR-HSI), $\mathcal{J} \in \Re^{W \times H \times b}$ to represent the MSI capturing the same scene with high spatial resolution (HR-MSI), and $\tilde{\mathcal{I}} \in \Re^{w \times h \times B}$ to represent the fused image (HR-HSI). Here, $W, H,$ and b are the three dimensions of the LR-HSI, while $w, h,$ and B are the three dimensions of the HR-MSI. The goal of HSI-MSI fusion is to obtain a HR-HSI $\tilde{\mathcal{I}}$ by fusing $\mathcal{I}$ and $\mathcal{J}$. The relationship between $\mathcal{I}$, $\mathcal{J}$, and $\tilde{\mathcal{I}}$ can be expressed as

$$\mathcal{I} = \tilde{\mathcal{I}}\, \mathcal{S}\mathcal{H} + \mathcal{E}_h \tag{3}$$

$$\mathcal{J} = \tilde{\mathcal{I}} \times_3 \mathrm{R} + \mathcal{E}_m \tag{4}$$

where $\mathcal{S}$ and $\mathcal{H}$ are the spatial blurring and down-sampling operators on the tensors, respectively, $\mathrm{R} \in \Re^{l \times B}$ is the spectral

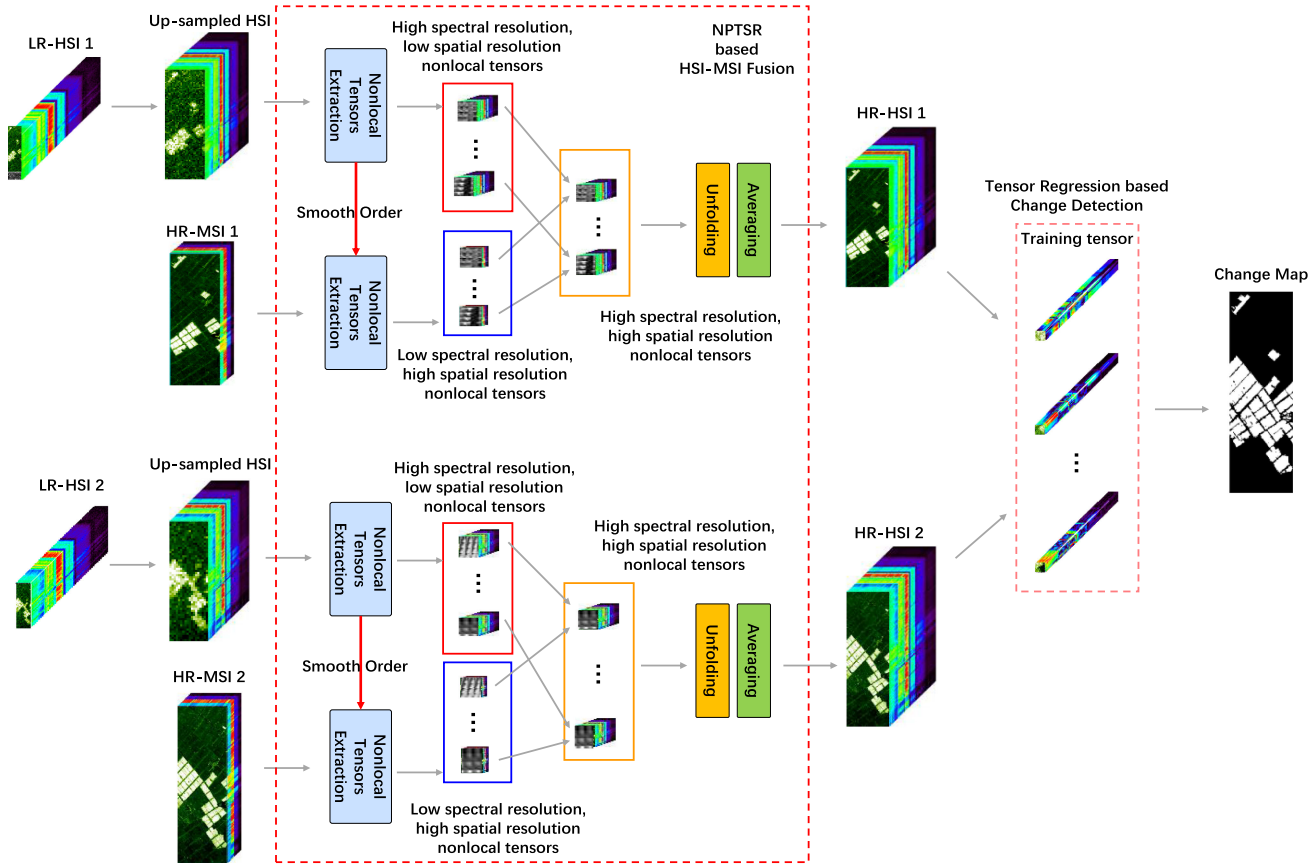

Fig. 1. Flow chart of the proposed method.

response of the multispectral sensor, and $\mathcal{E}_h$ and $\mathcal{E}_m$ represent i.i.d. noise. $\tilde{\mathcal{I}}\times_3\mathrm{R}$ in (4) represents the three-mode product of tensor $\tilde{\mathcal{I}}$ and a matrix R. The following equation represents the three-mode product using elements in the tensor and the matrix

$$\tilde{\mathcal{I}}\times_3\mathrm{R}\ (i_1,i_2,m)=\sum_{i_3}\tilde{\mathcal{I}}\,(i_1,i_2,m)\ \mathrm{R}\,(m,i_3)\,. \tag{5}$$

C. Change Detection

The task of change detection involves using images of the same scene from two or more time points to detect changes that occur at different time points. Here, we consider the change detection between images captured at two time points. If $\tilde{\mathcal{I}}_1$ and $\tilde{\mathcal{I}}_2$ are the HSI-MSI fusion images at two different time points, we can calculate their difference as follows:

$$\Delta\,\tilde{\mathcal{J}}=\left|\tilde{\mathcal{I}}_1-\tilde{\mathcal{I}}_2\right| \tag{6}$$

where $\Delta\tilde{\mathcal{J}}\in\Re^{W\times H\times B}$ is the difference image of $\tilde{\mathcal{I}}_1$ and $\tilde{\mathcal{I}}_2$. Thereafter, the classification method can be applied to obtain the change area from the difference image.

III. Our Method

In this methodology, we initially use NCTCP to perform HSI-MSI fusion. Then, the difference image is obtained by subtracting the fused image at two different time points. The tensor is then extracted from the difference image and a binary classification method based on tensor regression is used to detect the change area. A flow chart of our methodology is presented in Fig. 1.

A. HSI-MSI Fusion

Let $\mathcal{I}_1,\mathcal{I}_2\in\Re^{w\times h\times b}$ represent the observed LR-HSIs at two different time points, $\mathcal{J}_1,\mathcal{J}_2\in\Re^{W\times H\times B}$ represent the HR-MSIs at two different time points, and $\tilde{\mathcal{I}}_1,\tilde{\mathcal{I}}_2\in\Re^{W\times H\times B}$ represent the fused images. The images at each time point are fused by using the NCTCP method [39] separately.

Let $\mathcal{G}_p\mathcal{Y}^1$ and $\mathcal{G}_p\mathcal{Y}^2$ represent the third-order tensors that combine all of the 2-D image patches of $\tilde{\mathcal{I}}_1$ and $\tilde{\mathcal{I}}_2$ in the pth cluster, they can be written as

$$\begin{aligned}\mathcal{G}_P\,\mathcal{Y}^1&=\mathcal{G}_P\,\tilde{\mathcal{J}}_1\times_3\mathbf{R}+\mathcal{G}_p\mathcal{E}_m^1\\&=\left[\left[\boldsymbol{A}_p^1,\boldsymbol{B}_p^1,\boldsymbol{C}_p^1\right]\right]\times_3\mathbf{R}+\mathcal{G}_p\mathcal{E}_m^1\\&=\left[\left[A_p^1,B_p^1,\mathrm{R}C_p^1\right]\right]+\mathcal{G}_p\mathcal{E}_m^1\end{aligned} \tag{7}$$

$$\begin{aligned}\mathcal{G}_P\,\mathcal{Y}^2&=\mathcal{G}_P\,\tilde{\mathcal{J}}_2\times_3\mathbf{R}+\mathcal{G}_p\mathcal{E}_m^2\\&=\left[\left[\boldsymbol{A}_p^2,\boldsymbol{B}_p^2,\boldsymbol{C}_p^2\right]\right]\times_3\mathbf{R}+\mathcal{G}_p\mathcal{E}_m^2\\&=\left[\left[A_p^2,B_p^2,\mathrm{R}C_p^2\right]\right]+\mathcal{G}_p\mathcal{E}_m^2.\end{aligned} \tag{8}$$

Thus, the NCTCP method extends the non-local patch similarity to the non-local tensor representation and generates HR-MSIs by solving the two following optimization problems

$$\min_{\tilde{\mathcal{J}}_1, \mathbf{A}_p^1, \mathbf{B}_p^1, \mathbf{C}_p^1} \left\{ \left\| \tilde{\mathcal{J}}_1 - \tilde{\mathcal{J}}_1 \mathcal{S}\mathcal{H} \right\|_F^2 + \mu \sum_{p=1}^{p} \left\| \mathcal{G}_p \mathcal{Y}^1 - [[\mathbf{A}_p^1, \mathbf{B}_p^1, \mathbf{R}\mathbf{C}_p^1]] \right\|_F^2 \right\}$$

$$s.t.\ \tilde{\mathcal{J}}_1 = \left(\sum_p \mathcal{G}_p^T \mathcal{G}_p \right)^{-1} \sum_p \mathcal{G}_P^T \left[[\mathbf{A}_p^1, \mathbf{B}_p^1, \mathbf{C}_p^1] \right] \quad (9)$$

$$\min_{\tilde{\mathcal{J}}_2, \mathbf{A}_p^2, \mathbf{B}_p^2, \mathbf{C}_p^2} \left\{ \begin{array}{l} \left\| \tilde{\mathcal{J}}_2 - \tilde{\mathcal{J}}_2 \mathcal{S}\mathcal{H} \right\|_F^2 + \mu \sum_{p=1}^{p} \\ \left\| \mathcal{G}_p \mathcal{Y}^2 - [[\mathbf{A}_p^2, \mathbf{B}_p^2, \mathbf{R}\mathbf{C}_p^2]] \right\|_F^2 \end{array} \right\}$$

$$s.t.\ \tilde{\mathcal{I}}_2 = \left(\sum_p \mathcal{G}_p^T \mathcal{G}_p \right)^{-1} \sum_p \mathcal{G}_P^T [\![\mathbf{A}_p^2, \mathbf{B}_p^2, \mathbf{C}_p^2]\!]. \quad (10)$$

The details for solving (9) and (10) are presented in [26]. We use Algorithm 1 from [26] to obtain two HR-HSIs, $\tilde{\mathcal{I}}_1$ and $\tilde{\mathcal{I}}_2$, at two time points.

B. Change Detection Using Tensor Regression

After obtaining $\tilde{\mathcal{I}}_1, \tilde{\mathcal{I}}_2 \in \Re^{W \times H \times B}$, the difference image $\Delta\tilde{\mathcal{J}}$ can be calculated according to (6). To detect the change region from $\Delta\tilde{\mathcal{J}}$, we use the generalized tensor regression method (GTR) [60] to divide $\Delta\tilde{\mathcal{J}}$ into two categories. By assuming that $\mathcal{A} \in \mathbb{R}^{W \times H \times b \times J}$ are training tensors and that $\mathcal{T} \in \mathbb{R}^{2 \times 1 \times \ldots \times 1 \times J}$ is the label tensor, the GTR method obtains the coefficient weights by solving the following optimization problems:

$$\min_{\mathbf{W}^{(n)}} \left\| \mathcal{T} - \mathcal{A} \prod_{n=1}^{3} \times_n \mathbf{W}^{(n)} \right\|_F^2 + \lambda \prod_{n=1}^{3} \left\| \mathbf{W}^{(n)} \right\|_F^2$$

$$\text{s.t. } \mathbf{W}^{(n)} \succeq 0,\ \mathrm{n} = 2, 3 \quad (11)$$

where $\mathbf{W}^{(n)} \succeq 0$ implies that all elements of $\mathbf{W}^{(n)}$ are nonnegative.

In [60], Liu *et al*. considered imposing a rank-R constraint in (11) to decrease the regression error by factorizing $\mathcal{W}_{c:} = \sum_{r=1}^{R} \mathcal{W}_{r,c:} = \mathbf{w}_{r,c:}^{(1)} \circ \mathbf{w}_r^{(2)} \circ \mathbf{w}_r^{(3)}$ and then performing model estimation by solving the following optimization problem:

$$\min_{\mathbf{W}_{r,c:}} \sum_{c,j} \left(t_{cj} - \mathcal{A}_{:j}, \sum_r \mathcal{W}_{r,c:} \right)^2 + \sum_{c,r} \lambda_r \left\| \mathbf{w}_{r,c:} \right\|_F^2$$

$$\text{s.t. } \mathcal{W}_{r,c:} = \mathbf{w}_{r,c:}^{(1)} \prod_{n=2}^{N} \circ \mathbf{w}_r^{(n)},\ \mathbf{w}_r^{(n)} \succeq 0,\ \mathrm{n} = 2, 3 \quad (12)$$

where $\{\lambda_r > 0 | \mathrm{r} = 1, 2, \cdots, \mathrm{R}\}$ are regularization parameters.

Algorithm 1

Input: LR-HSIs: $\mathcal{I}_1, \mathcal{I}_2 \in \Re^{w \times h \times b}$; HR-MSIs: $\mathcal{J}_1, \mathcal{J}_2 \in \Re^{W \times H \times B}$; positions and labels of training samples;
Obtain $\tilde{\mathcal{I}}_1$ by fusing $\mathcal{I}_1$ and $\mathcal{J}_1$ using the NCTCP method presented in Section III.A;
Obtain $\tilde{\mathcal{I}}_2$ by fusing $\mathcal{I}_2$ and $\mathcal{J}_2$ using the NCTCP method presented in Section III.A;
Calculate the difference image $\Delta\tilde{\boldsymbol{\mathcal{J}}}$;
Generate the tensors of training samples $\boldsymbol{\mathcal{A}}$ and their label tensors $\boldsymbol{\mathcal{T}}$;
Detect the change region from $\Delta\tilde{\boldsymbol{\mathcal{J}}}$ using the GTR method presented in Section III.B;
Output: The change detection result.

We divide the difference image $\Delta\tilde{\mathcal{J}}$ into several small tensors $\Delta\tilde{\mathcal{J}}_i \in \Re^{W_p \times H_p \times b}, i = 1, 2, \ldots, n$, where the label of each tensor can be determined by

$$y = \mathrm{argmax}_{c=1,2}\ \delta_c \left(\sum_r \Delta\tilde{\mathcal{J}}_i \prod_{n=1}^{3} \times_n \mathbf{w}_r^{(n)} \right) \quad (13)$$

where $\mathbf{W}_r^{(1)} = [\mathbf{w}_{r,1:}^{(1)}, \mathbf{w}_{r,2:}^{(1)}]^{\boldsymbol{T}}$ and $\mathbf{W}_r^{(n)} = (\mathbf{W}_r^{(n)})^{\boldsymbol{T}}$ $(\mathrm{n} \in \{2, 3\})$.

C. Algorithm Procedure

The procedure for the proposed algorithm is provided as follows.

IV. Experiments

In this section, we first describe the datasets and metrics used to evaluate change detection in this comparison experiment. Then, we introduce the experimental results obtained by our method and compare them to other competitive methods.

A. Datasets

Three HSIs were used to simulate the datasets. First, we extracted the four corresponding bands from the HSIs to form multispectral data. Then, we reduced the lengths and widths of the HSIs to half of their original size to form hyperspectral data. The details of these datasets are presented as follows.

The Farmland dataset [61] contains images of a farmland area in Yancheng City, Jiangsu Province, China. The two groups of hyperspectral data (see Fig. 2) in this dataset were collected by the earth observing-1 (EO-1) hyperspectral imager on May 3, 2006 and April 23, 2007, respectively. The spatial size of this dataset is 450×140, and the number of spectral bands is 155. Cultivated land changes represent the main changes in this dataset. The 24th to 26th bands, 37th to 39th bands, 92nd to 94th bands, and 141st to 143rd bands were selected, and their mean values were calculated to simulate the MSIs with high spatial resolution, while the correspondingp LR-HSI was generated via down-sampling.

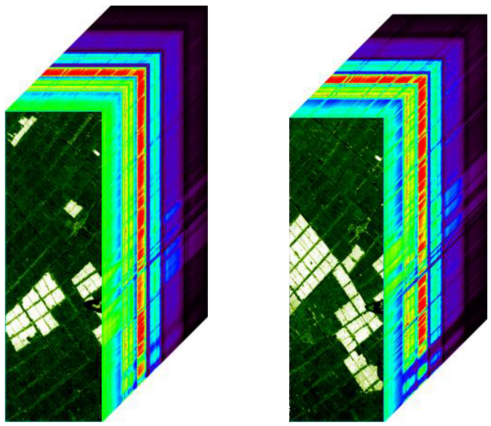

Fig. 2. Farmland dataset.

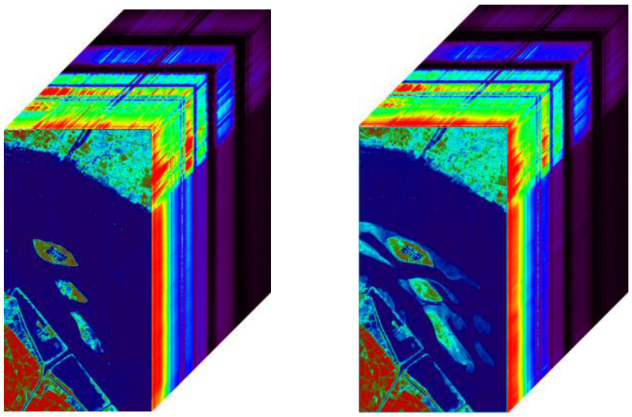

Fig. 3. River dataset.

1) River Dataset: The River dataset [62] contains images of a river area in Jiangsu Province, China. The two groups of hyperspectral data (see Fig. 3) in this dataset were collected by the EO-1hyperspectral imager on May 3, 2013 and December 31, 2013, respectively. The spatial size of this dataset is 200×100, and the number of spectral bands is 198. Crop and land changes in irrigated farmland represent the main changes in this dataset. The 24th to 26th bands, 37th to 39th bands, 92nd to 94th bands, and 141st to 143rd bands were selected, and their mean values were calculated to simulate the MSIs with high spatial resolution, while the corresponding LR-HSI was generated via down-sampling.

2) USA Dataset: The USA dataset [63] contains images of an irrigated farmland area in Hermiston, Umatilla County, Oregon, USA. The two groups of hyperspectral data (see Fig. 4) in this dataset were collected by the EO-1 hyperspectral imager. The spatial size of this dataset is 300×240, and the number of spectral bands is 154. Material changes in the river and land changes around the river represent the main changes in this dataset. The 14th to 16th bands, 37th to 39th bands, 92nd to 94th bands and 141st to 143rd bands were selected, and their mean values were calculated to simulate the MSIs with high spatial resolution, while the corresponding LR-HSI was generated via down-sampling.

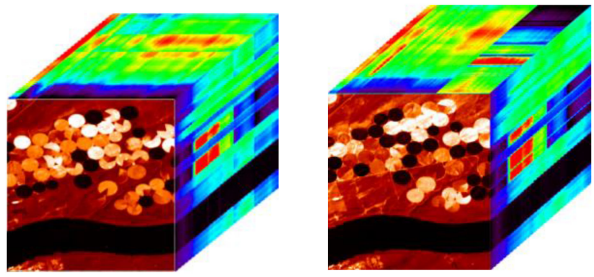

Fig. 4. USA dataset.

B. Quality Measures

A confusion matrix is commonly used to evaluate the effect of classification. Considering a hyperspectral two-classification change detection problem with a spatial size of $\mathrm{h} \times \mathrm{w}$, the detection result may only appear as one of the following four situations: the number of changed pixels that are correctly classified is recorded as TP; the number of unchanged pixels that are correctly classified is recorded as TN; the number of changed pixels that are incorrectly classified is recorded as FN; the number of unchanged pixels that are incorrectly classified is recorded as FP. Therefore

$$\mathrm{TP} + \mathrm{TN} + \mathrm{FP} + \mathrm{FN} = hw. \tag{14}$$

The initial evaluation index used in this experiment is overall accuracy (OA), which is used to evaluate the proportion of pixels that are correctly classified

$$\mathrm{OA} = \frac{\mathrm{TP} + \mathrm{TN}}{hw}. \tag{15}$$

The second evaluation index is the average accuracy (AA), which is used to evaluate the proportion of pixels that are correctly classified in each category

$$\mathrm{AA} = \frac{1}{2}\left(\frac{\mathrm{TN}}{\mathrm{TN}+\mathrm{FP}} + \frac{\mathrm{TP}}{\mathrm{TP}+\mathrm{FN}}\right). \tag{16}$$

The third evaluation index is the kappa coefficient, which combines the diagonal and off-diagonal terms of the confusion matrix and is a robust consistency measure

$$\mathrm{Kappa} = \frac{1-p}{OA-p} \tag{17}$$

$$p = \frac{(\mathrm{TP}+\mathrm{FP})(\mathrm{TP}+\mathrm{FN}) + (\mathrm{TN}+\mathrm{FP})(\mathrm{TN}+\mathrm{FN})}{h^2 w^2}. \tag{18}$$

C. Parameter Selection

To simulate the LR-HSIs, the HSIs are downsampled by selecting one pixel from a patch with a size of 5×5. According to the parameter analysis presented in [39], the balance parameter μ, rank, and number of patches used for image fusion are set as 100, 8, and 300, respectively. Three parameters are included in

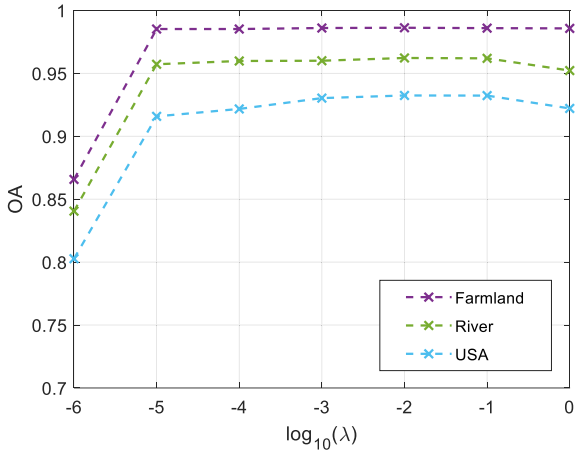

Fig. 5. OA values for three datasets with varying λ values.

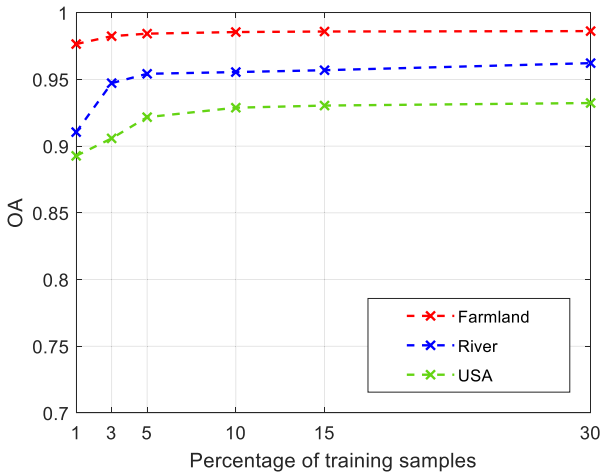

Fig. 6. OA values for three datasets with different training samples.

the change detection process. The rank used for classification is set as 1 [60]. The parameter λ is used to maintain a balance between the fidelity and regularization terms. Fig. 5 demonstrates the impact of λ on the change detection process. Based on the results, the optimal value can be chosen from [1 0-1, 10-6]. Notably, the number of training samples is very important for change detection. Fig. 6 illustrates the OA values for a varying number of training samples. Based on this figure, it is evident that our change detection method can obtain stable and effective change detection accuracy by using only 3% of the samples selected as training samples.

D. Experimental Results

To verify the effectiveness of the proposed method, we conducted the following comparative methods as an experiment: support vector machine (SVM) [64], GETNET [62], and Hybrid-SN [65]. These methods are commonly used to perform change detection using MSIs, with image fusion being performed separately. Thereafter, the OA, AA, and kappa values were calculated

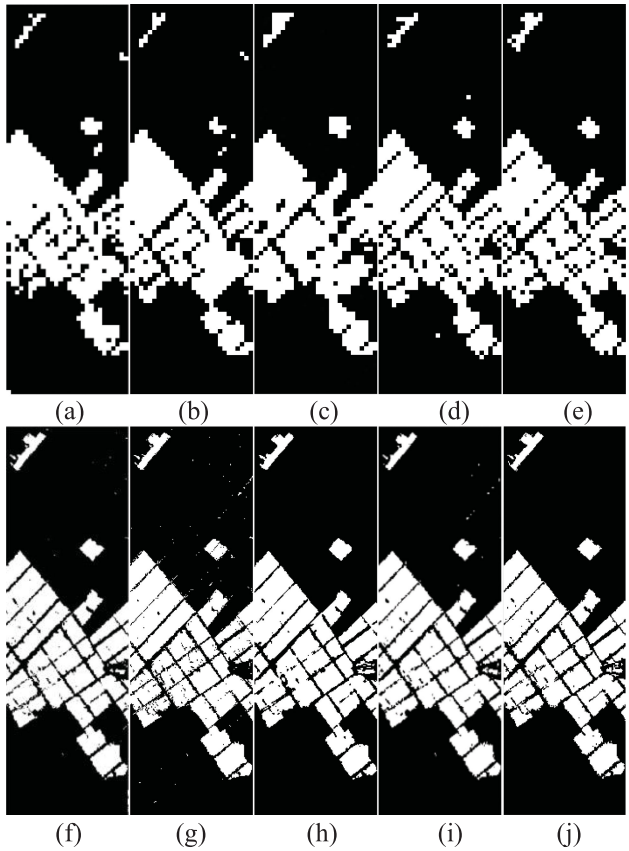

Fig. 7. CRS results for the Farmland dataset. (a) SVM-MSI. (b) GETNET-MSI. (c) Hybrid-SN-MSI. (d) TRIFCD-MSI. (e) Ground truth-MSI. (f) SVM-HR-HIS; (g) GETNET- HR-HIS. (h) Hybrid-SN- HR-HIS. (i) TRIFCD- HR-HIS. (j) Ground truth-HIS.

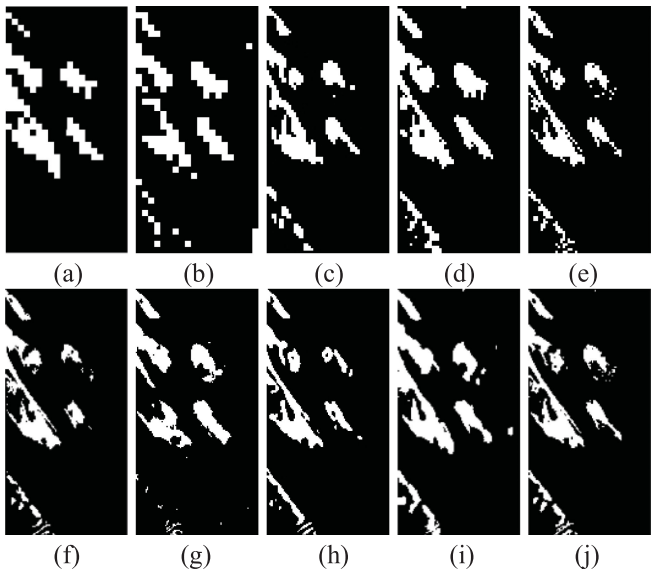

Fig. 8. CRS results for the River dataset. (a) SVM-MSI. (b) GETNET-MSI. (c) Hybrid-SN-MSI. (d) TRIFCD-MSI. (e) TRIFCD-MSI. (f) SVM-HR-HIS. (g) GETNET- HR-HIS. (h) Hybrid-SN- HR-HIS. (i) TRIFCD- HR-HIS. (j) Ground truth-HIS.

TABLE I
QUANTITATIVE ANALYSIS OF TRIFCD AND OTHER ADVANCED CHANGE DETECTION METHODS FOR THREE DATASETS

Method	Index	Experimental datasets					
		Farmland-MS	Farmland-Fusion	River-MS	River-Fusion	USA-MS	USA-Fusion
SVM	OA	0.9496	0.9803	0.9312	0.9500	0.8812	0.9134
	AA	0.9412	0.9791	0.8022	0.8866	0.8501	0.9286
	Kappa	0.8786	0.9521	0.6708	0.7331	0.6149	0.7209
GETNET	OA	0.9555	0.9708	0.9200	0.9460	0.8722	0.9086
	AA	0.9499	0.9614	0.7778	0.8650	0.8429	0.9161
	Kappa	0.8926	0.9298	0.6326	0.7229	0.6103	0.7113
Hybrid-SN	OA	0.9186	0.9738	0.9375	0.9408	0.8638	0.9100
	AA	0.9073	0.9694	0.7430	0.8413	0.8364	0.8959
	Kappa	0.8069	0.9365	0.5833	0.6942	0.6012	0.7573
TRIFCD	OA	**0.9754**	**0.9818**	**0.9442**	**0.9529**	**0.8848**	**0.9263**
	AA	**0.9724**	**0.9781**	**0.9364**	**0.9489**	**0.9076**	**0.9151**
	Kappa	**0.9408**	**0.9558**	**0.7063**	**0.7573**	**0.7024**	**0.7813**

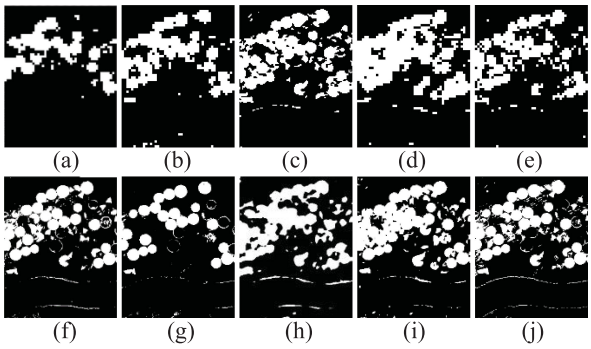

Fig. 9. CRS results for the USA dataset. (a) SVM-MSI. (b) GETNET-MSI. (c) Hybrid-SN-MSI. (d) TRIFCD-MSI. (e) Ground truth-MSI. (f) SVM-HR-HIS. (g) GETNET- HR-HIS. (h) Hybrid-SN- HR-HIS. (i) TRIFCD- HR-HIS. (j) Ground truth-HIS.

according to (15) to (17). Figs. 7–9 demonstrate the change detection results obtained via different methods of processing MSIs and fusion images. Table I gives the quantitative analysis results for the different methods executed on the MSIs and fusion images. The results indicate that the method proposed in this article can achieve optimal change detection results for both MSIs and fusion images, which highlights the advantages of this method in terms of change detection. Additionally, the image fusion process also improves the change detection results, which demonstrates that the technical solution proposed in this article is very effective when both LR-HSIs and HR-HSIs are available. Table II gives the running time of the proposed method carried out in Intel Core 2.59GHz processor with 8-GB memory. It can be seen that the running time of our method is within [130s, 180s]. This quantitative result demonstrates our method is very efficient and does not require GPU support, although GPU can further improve the efficiency of our proposed method.

TABLE II
RUNNING TIMES OF TRIFCD (SECONDS) ON THREE DATASETS

Algorithm	Farmland	River	USA
NCTCP-based Fusion	129.79	173.55	154.81
GTR-based change detection	2.12	3.73	1.23
TRIFCD	132.87	178.86	156.62

V. CONCLUSION

In this article, we propose a TRIFCD method. First, NCTCP is applied to perform HSI-MSI fusion. By subtracting the fused HR-HSIs, the change detection problem is transformed into two binary classification problems on the difference image. Thus, a tensor regression-based method is used to classify the difference

image to detect the final change result. The fusion of LR-HSI and HR-MSI improves image resolution and thus further improves the accuracy of change detection. Using tensor representation in the method can maintain the intrinsic spectral-spatial structure of an image and overcome the effects of image degradation. Moreover, the GTR classifier used for change detection in the difference map is a simple and stable classifier that can obtain change detection results more stably and efficiently. The proposed method has been experimentally tested using three different datasets, with the results demonstrating that this method provides improved change detection performance on all datasets when compared to existing state-of-art change detection methods.

REFERENCES

[1] S. Montariol, M. Martinc, and L. Pivovarova, "Scalable and interpretable semantic change detection," in *Proc. Conf. North Amer. Chapter Assoc. Comput. Linguistics, Hum. Lang. Technol.*, Jun. 2021, pp. 4642–4652.

[2] L. Zhang, X. Hu, M. Zhang, Z. Shu, and H. Zhou, "Object-level change detection with a dual correlation attention-guided detector," *ISPRS J. Photogramm. Remote Sens.*, vol. 177, pp. 147–160, 2021.

[3] V. Krishnamurthy, "Quickest change detection with time inconsistent anticipatory agents in cyber-physical systems," in *Proc. IEEE Int. Conf. Acoust., Speech Signal Process*, 2021, pp. 5000–5004.

[4] F. Bovolo and L. Bruzzone, "The time variable in data fusion: A change detection perspective," *IEEE Geosci. Remote Sens. Mag.*, vol. 3, no. 3, pp. 8–26, Sep. 2015.

[5] L. Xie, S. Zou, Y. Xie, and V. V. Veeravalli, "Sequential (Quickest) change detection: Classical results and new directions," *IEEE J. Sel. Areas Inf. Theory.*, vol. 2, no. 2, pp. 494–514, Jun. 2021.

[6] K. Song and J. Jiang, "AGCDetNet: An attention-guided network for building change detection in high-resolution remote sensing images," *IEEE J. Sel. Topics Appl. Earth Observ. Remote Sens.*, vol. 14, pp. 4816–4831, 2021.

[7] Q. Guo, J. Zhang, C. Zhong, and Y. Zhang, "Change detection for hyperspectral images via convolutional sparse analysis and temporal spectral unmixing," *IEEE J. Sel. Topics Appl. Earth Observ. Remote Sens.*, vol. 14, pp. 4417–4426, Apr. 2021.

[8] H. Wang, J. Qi, Y. Lei, J. Wu, B. Li, and Y. Jia, "A refined method of high-resolution remote sensing change detection based on machine learning for newly constructed building areas," *Remote Sens.,* vol. 13, no. 8, 2021, Art. no 1507.

[9] N. Bouhlel, V. Akbari, and S. Méric, "Change detection in multilook polarimetric SAR imagery with determinant ratio test statistic," *IEEE Trans. Geosci. Remote Sens.*, to be published, doi: 10.1109/TGRS.2020.3043517.

[10] M. Yang, L. Jiao, F. Liu, B. Hou, S. Yang, and M. Jian, "DPFL-Nets: Deep pyramid feature learning networks for multiscale change detection," *IEEE Trans. Neural Netw. Learn. Syst.*, to be published, doi: 10.1109/TNNLS.2021.3079627.

[11] J. Prexl, S. Saha, and X. X. Zhu, "Mitigating spatial and spectral differences for change detection using super-resolution and unsupervised learning," in *Proc. Int. Geosci. Remote Sens. Symp.*, 2021, pp. 1–4.

[12] D. Wang, X. Chen, M. Jiang, S. Du, B. Xu, and J. Wang, "ADS-Net: An attention-based deeply supervised network for remote sensing image change detection," *Int. J. Appl. Earth Observ. GeoInf.*, vol. 101, 2021, Art. no. 102339.

[13] C. Change, "An effectiove evaluation tool for hyperspectral target detection: 3D receiver operating characteristic curve analysis," *IEEE Trans. Geosci. Remote Sens.*, vol. 59, no. 6, pp. 5131–5153, Jun. 2021.

[14] D. Hong, L. Gao, J. Yao, B. Zhang, A. Plaza, and J. Chanussot, "Graph convolutional networks for hyperspectral image classification," *IEEE Trans. Geosci. Remote Sens.*, vol. 59, no. 7, pp. 5966–5978, Jul. 2021.

[15] C. Change, "Hyperspectral target detection: Hypothesis testing, signal-to-noise ratio, and spectral angle theories," *IEEE Trans. Geosci. Remote Sens.*, to be published, doi: 10.1109/TGRS.2021.3069716.

[16] D. Hong *et al.*, "More diverse means better: Multimodal deep learning meets remote-sensing imagery classification," *IEEE Trans. Geosci. Remote Sens.*, vol. 59, no. 5, pp. 4340–4354, May 2021.

[17] D. Hong, N. Yokoya, J. Chanussot, and X. X. Zhu, "An augmented linear mixing model to address spectral variability for hyperspectral unmixing," *IEEE Trans. Image Process.*, vol. 28, no. 4, pp. 1923–1938, Apr. 2019.

[18] J. Li, J. M. Bioucas-Dias, and A. Plaza, "Exploiting spatial information in semi-supervised hyperspectral image segmentation," in *Proc. 2nd Workshop Hyperspectral Image Signal Process., Evol. Remote Sens.*, 2010, pp. 1–4.

[19] Q. Ye, J. Yang, F. Liu, C. Zhao, N. Ye, and T. Yin, "L1-norm distance linear discriminant analysis based on an effective iterative algorithm," *IEEE Trans. Circuits Syst. for Video Technol.*, vol. 28, no. 1, pp. 114–129, Jan. 2018.

[20] L. Fu *et al.*, "Learning robust discriminant subspace based on joint L2, p- and L2, s-Norm distance metrics," *IEEE Trans. Neural Netw. Learn. Syst.*, to be published, doi: 10.1109/TNNLS.2020.3027588.

[21] C.-I. Chang, H. Cao, and M. Song, "Orthogonal subspace projection target detector for hyperspectral anomaly detection," *IEEE J. Sel. Topics Appl. Earth Observ. Remote Sens.*, vol. 14, pp. 4915–4932, 2021.

[22] C.-I. Chang and J. Chen, "Orthogonal subspace projection using data sphering and low-rank and sparse matrix decomposition for hyperspectral target detection," *IEEE Trans. Geosci. Remote Sens.*, vol. 59, no. 10, pp. 8704–8722, Oct. 2021.

[23] D. Hong *et al.*, "Interpretable hyperspectral artificial intelligence: When nonconvex modeling meets hyperspectral remote sensing," *IEEE Geosci. Remote Sens. Mag.*, vol. 9, no. 2, pp. 52–87, Jun. 2021.

[24] D. Hong, N. Yokoya, J. Chanussot, J. Xu, and X. X. Zhu, "Joint and progressive subspace analysis (JPSA) with spatial–spectral manifold alignment for semisupervised hyperspectral dimensionality reduction," *IEEE Trans. Cybern.*, vol. 51, no. 7, pp. 3602–3615, Jul. 2021.

[25] Q. Wei, J. Bioucas-Dias, N. Dobigeon, and J. Tourneret, "Hyperspectral and multispectral image fusion based on a sparse representation," *IEEE Trans. Geosci. Remote Sens.*, vol. 53, no. 7, pp. 3658–3668, Jul. 2015.

[26] T. Zhang *et al.*, "HOG-ShipCLSNet: A novel deep learning network with HOG feature fusion for SAR ship classification," *IEEE Trans. Geosci. Remote Sens.*, to be published, doi: 10.1109/tgrs.2021.3082759.

[27] H. Gao *et al.*, "cuFSDAF: An enhanced flexible spatiotemporal data fusion algorithm parallelized using graphics processing units," *IEEE Trans. Geosci. Remote Sens.*, to be published, doi: 10.1109/TGRS.2021.3080384.

[28] J. Choi, K. Yu, and Y. Kim, "A new adaptive component-substitution-based satellite image fusion by using partial replacement," *IEEE Trans. Geosci. Remote Sens.*, vol. 49, no. 1, pp. 295–309, Jan. 2011.

[29] Y. Yang, Y. Zhang, S. Huang, Y. Zuo, and J. Sun, "Infrared and visible image fusion using visual saliency sparse representation and detail injection model," *IEEE Trans. Instrum. Meas.*, vol. 70, pp. 1–15, 2021, Art no. 5001715, doi: 10.1109/TIM.2020.3011766.

[30] Q. Wei, J. Bioucas-Dias, N. Dobigeon, J. Tourneret, M. Chen, and S. Godsill, "Multiband image fusion based on spectral unmixing," *IEEE Trans. Geosci. Remote Sens.*, vol. 54, no. 12, pp. 7236–7249, Dec. 2016.

[31] H. Li, X. Wu, and J. Kittler, "Infrared and visible image fusion using a deep learning framework," in *Proc. 24th Int. Conf. Pattern Recognit.*, 2018, pp. 2705–2710.

[32] H. Wang, S. Li, L. Song, L. Cui, and P. Wang, "An enhanced intelligent diagnosis method based on multi-sensor image fusion via improved deep learning network," in *IEEE Trans. Instrum. Meas.*, vol. 69, no. 6, pp. 2648–2657, Jun. 2020.

[33] Z. Shao, J. Cai, P. Fu, L. Hu, and T. Liu, "Deep learning-based fusion of Landsat-8 and Sentinel-2 images for a harmonized surface reflectance product," *Remote Sens. Environ.*, vol. 235, 2019, Art. no. 111425.

[34] J H. Jung, Y. Kim, H. Jang, N. Ha, and K. Sohn, "Unsupervised deep image fusion with structure tensor representations," *IEEE Trans. Image Process.*, vol. 29, pp. 3845–3858, Jan. 2020.

[35] Y. Xu, Z. Wu, J. Chanussot, P. Comon, and Z. Wei, "Nonlocal coupled tensor CP decomposition for hyperspectral and multispectral image fusion," *IEEE Trans. Geosci. Remote Sens.*, vol. 58, no. 1, pp. 348–362, Jan. 2020.

[36] X. Li, Y. Yuan, and Q. Wang, "Hyperspectral and multispectral image fusion via nonlocal low-rank tensor approximation and sparse representation," *IEEE Trans. Geosci. Remote Sens.*, vol. 59, no. 1, pp. 550–562, Jan. 2021.

[37] S. Li, R. Dian, L. Fang, and J. M. Bioucas-Dias. Bioucas-Dias, "Fusing hyperspectral and multispectral images via coupled sparse tensor factorization," *IEEE Trans. Image Process*, vol. 27, no. 8, pp. 4118–4130, Aug. 2018.

[38] C. I. Kanatsoulis, X. Fu, N. D. Sidiropoulos, and W. Ma, "Hyperspectral super-resolution via coupled tensor factorization: Identifiability and algorithms," in *Proc. IEEE Int. Conf. Acoust. Speech Signal Process*, 2018, pp. 3191–3195.

[39] Y. Xu, Z. Wu, J. Chanussot, P. Comon, and Z. Wei, "Nonlocal coupled tensor CP decomposition for hyperspectral and multispectral image fusion," *IEEE Trans. Geosci. Remote Sens.*, vol. 58, no. 1, pp. 348–362, Jan. 2020.
[40] W. A. Malila, "Change vector analysis: An approach for detecting forest changes with landsat," in *Proc. Mach. Process. Remotely Sensed Data Symp.*, 1980, vol. 29, pp. 326–335.
[41] A. A. Nielsen, K. Conradsen, and J. J. Simpson, "Multivariate alteration detection (MAD) and MAF postprocessing in multispectral, bitemporal image data: New approaches to change detection studies," *Remote Sens. Environ.*, vol. 64, no. 1, pp. 1–19, 1998.
[42] A. A. Nielsen, "The regularized iteratively reweighted MAD method for change detection in multi- and hyperspectral data," *IEEE Trans. Image Process.*, vol. 16, no. 2, pp. 463–478, Feb. 2007.
[43] F. Huang, Y. Yu, and T. Feng, "Hyperspectral remote sensing image change detection based on tensor and deep learning," *J. Vis. Commun. Image Representation*, vol. 58, pp. 233–244, 2019.
[44] X. Chen, J. Chen, Y. Shi, and Y. Yamaguchi, "An automated approach for updating land cover maps based on integrated change detection and classification methods," *ISPRS J. Photogramm. Remote Sens.*, vol. 71, pp. 86–95, 2012.
[45] Y. Hu and Y. Dong, "An automatic approach for land-change detection and land updates based on integrated NDVI timing analysis and the CVAPS method with GEE support," *ISPRS J. Photogramm. Remote Sens.*, vol. 146, pp. 347–359, 2018.
[46] H. Zhang, M. Gong, P. Zhang, L. Su, and J. Shi, "Feature-level change detection using deep representation and feature change analysis for multispectral imagery," *IEEE Geosci. Remote Sens. Lett.*, vol. 13, no. 11, pp. 1666–1670, Nov. 2016.
[47] W. Yu, M. Zhang, and Y. Shen, "Learning a local manifold representation based on improved neighborhood rough set and LLE for hyperspectral dimensionality reduction," *Signal Process,* vol. 164, pp. 20–29, 2019.
[48] N. Lv, C. Chen, T. Qiu, and A. K. Sangaiah, "Deep learning and superpixel feature extraction based on contractive autoencoder for change detection in SAR images," *IEEE Trans. Ind. Informat.*, vol. 14, no. 12, pp. 5530–5538, Dec. 2018.
[49] W. Wang, S. Dou, Z. Jiang, and L. Sun, "A fast dense spectral–spatial convolution network framework for hyperspectral images classification," *Remote Sens,* vol. 10, no. 7, 2018, Art. no. 1068.
[50] X. Wang, S. Liu, P. Du, H. Liang, J. Xia, and Y. Li, "Object-based change detection in urban areas from high spatial resolution images based on multiple features and ensemble learning," *Remote Sens,* vol. 10, no. 2, 2018, Art. no. 276.
[51] P. Xiao, X. Zhang, D. Wang, M. Yuan, X. Feng, and M. Kelly, "Change detection of built-up land: A framework of combining pixel-based detection and object-based recognition," *ISPRS J. Photogramm. Remote Sens.*, vol. 119, pp. 402–414, 2016.
[52] L. Xu, W. Jing, H. Song, and G. Chen, "High-resolution remote sensing image change detection combined with pixel-level and object-level," *IEEE Access*, vol. 7, pp. 78909–78918, 2019.
[53] T. Leichtle, C. Geiß, M. Wurm, T. Lakes, and H. Taubenböck, "Unsupervised change detection in VHR remote sensing imagery–An object-based clustering approach in a dynamic urban environment," *Int. J. Appl. Earth Observ. GeoInf.*, vol. 54, pp. 15–27, 2017.
[54] L. Ma *et al.*, "Object-based change detection in urban areas: The effects of segmentation strategy, scale, and feature space on unsupervised methods," *Remote Sens,* vol. 8, no. 9, 2016, Art. no. 761.
[55] Y. Xu, Z. Wu, J. Chanussot, and Z. Wei, "Hyperspectral images super-resolution via learning high-order coupled tensor ring representation," *IEEE Trans. Neural Netw. Learn. Syst.*, vol. 31, no. 11, pp. 4747–4760, Nov. 2020.
[56] F. Huang, Y. Yu, and T. Feng, "Hyperspectral remote sensing image change detection based on tensor and deep learning," *J. Vis. Commun. Image Representation*, vol. 58, pp. 233–244, 2019.
[57] S. Saritha and G. S. Kumar, "Change detection in urban landscapes: A tensor factorization approach," *Spatial Inf. Res.*, vol. 27, no. 5, pp. 587–600, 2019.
[58] F. Zhou and Z. Chen, "Hyperspectral image change detection by self-supervised tensor network," in *Proc. IEEE Int. Geosci. Remote Sens. Symp.*, 2020, pp. 2527–2530.
[59] H. Chen and Z. Shi, "A spatial-temporal attention-based method and a new dataset for remote sensing image change detection," *Remote Sens.,* vol. 12, no. 10, 2020, Art. no. 1662.
[60] J. Liu, Z. Wu, L. Xiao, J. Sun, and H. Yan, "Generalized tensor regression for hyperspectral image classification," *IEEE Trans. Geosci. Remote Sens.*, vol. 58, no. 2, pp. 1244–1258, Feb. 2020.
[61] Y. Yuan, H. Lv, and X. Lu, "Semi-supervised change detection method for multi-temporal hyperspectral images," *Neurocomputing*, vol. 148, pp. 363–375, 2015.
[62] Q. Wang, Z. Yuan, Q. Du, and X. Li, "GETNET: A general end-to-end 2-D CNN framework for hyperspectral image change detection," *IEEE Trans. Geosci. Remote Sens.*, vol. 57, no. 1, pp. 3–13, Jan. 2019.
[63] M. Hasanlou and S. T. Seydi, "Hyperspectral change detection: An experimental comparative study," *Int. J. Remote Sens.*, vol. 39, no. 20, pp. 7029–7083, 2018.
[64] H. Nemmour and Y. Chibani, "Multiple support vector machines for land cover change detection: An application for mapping urban extensions," *ISPRS J. Photogramm. Remote Sens.*, vol. 61, no. 2, pp. 125–133, 2006.
[65] S. K. Roy, G. Krishna, S. R. Dubey, and B. B. Chaudhuri, "HybridSN: Exploring 3-D–2-D CNN feature hierarchy for hyperspectral image classification," *IEEE Geosci. Remote Sens. Lett.*, vol. 17, no. 2, pp. 277–281, Feb. 2020.

Tianming Zhan received the B.S. and M. S. degrees in applied mathematics in 2006 and 2009, respectively, from the School of Math and Statistics, Nanjing University of Information Science and Technology, Nanjing, China, where he received the Ph.D. degree in patten recognition and intelligence system with the School of Computer Science and Engineering in 2013.

He is currently an Associated Professor with the School of Information Engineering, Nanjing Audit University Nanjing, China. His research interests include hyperspectral image processing, machine learning, and data analysis.

Yanwen Sun received the B.S. degree in computer science and technology from Pujiang College of Nanjing University of Technology, Nanjing, China, in 2020. She is currently working toward the M.S. degree in computer science and technology with Nanjing Audit University Nanjing, China.

Her research interests include object detection, Target tracking.

Yongsheng Tang received the B.S. degree in digital media technology from Jiangsu University of Technology, Changzhou, China, in 2020. He is currently working toward the M.S. degree in electronic information with Nanjing Audit University, Nanjing, China.

His research interests include hyperspectral image processing.

Yang Xu received the B.Sc. degree in applied mathematics and the Ph.D. degree in pattern recognition and intelligence systems from Nanjing University of Science and Technology (NUST), Nanjing, China, in 2011 and 2016, respectively.

He is currently an Associate Professor with the School of Computer Science and Engineering, NUST. His research interests include hyperspectral image classification, hyperspectral detection, image processing and machine learning.

Zebin Wu (Senior Member, IEEE) received the B.S. and Ph. D. degrees in computer science from Nanjing University of Science and Technology (NUST), Nanjing, China, in 2003 and 2007, respectively.

He is currently a Professor with the School of Computer Science and Engineering, NUST. His research interests include hyperspectral image processing, high-performance computing, and computer simulation.